Paleoceanography and Paleoclimatology

Supporting Information for

The Novel Hydroxylated Tetraether Index RI-OH' as a Sea Surface Temperature Proxy for the 160–45 ka BP Period Off the Iberian Margin

Nina Davtian[1]*, Edouard Bard[1], Sophie Darfeuil[1]†, Guillemette Ménot[2], and Frauke Rostek[1]

[1]CEREGE, Aix-Marseille University, CNRS, IRD, INRAE, Coll France, Technopôle de l'Arbois, Aix-en-Provence, France

[2]Univ Lyon, ENS de Lyon, Université Lyon 1, CNRS, UMR 5276 LGL-TPE, Lyon, France

*Now at Institut de Ciència i Tecnologia Ambientals (ICTA-UAB), Universitat Autònoma de Barcelona, Bellaterra, Spain

†Now at Univ Grenoble Alpes, CNRS, IRD, Grenoble Institute of Engineering and Management Univ Grenoble Alpes, IGE, Grenoble, France

Contents of this file

Additional Supporting Information (Files uploaded separately)

Introduction

The Supporting Information contains 14 Figures, 5 Tables, and 4 Data Set captions. Figure S1 provides the structures of the quantified archaeal lipids. Figures S2 and S3 show the age model, which uses the tie points shown in Tables S1 and S2. Figure S4 is similar to Figure 2, but with RI-OH. Figure S5 is similar to Figure 3, but with biomarker concentration results for other lipid classes. Figure S6 shows RI-OH(') versus $U^{K'}_{37}$ and

RI-OH(') versus TEX_{86} crossplots, with *r* values also shown in Table S4. Figure S7 is similar to Figure 5, but with RI-OH-SSTs. Figure S8 is similar to Figure S6, but with biomarker based-SSTs. Figure S9 is similar to Figure S8, but with Bayesian TEX_{86}-SST and $U^{K'}_{37}$-SST estimates. Figure S10 is similar to Figure 6, but with latitudinal SST gradients from RI-OH. Figure S11 is similar to Figures 6 and S10, but with latitudinal gradients from Bayesian TEX_{86}-SST and $U^{K'}_{37}$-SST estimates. Figure S12 is similar to Figure 7, but with RI-OH and summed OH-GDGT-1 and OH-GDGT-2 concentrations. Figure S13 compares the theoretical with observed bioturbation effect on RI-OH'-SST and $U^{K'}_{37}$-SST changes during a given Heinrich-like cold event. Figure S14 shows [2]/[3] versus TEX_{86}, water depth, and SST crossplots for Iberian Margin core and surface sediments as well as suspended particulate matter. Table S3 shows averaged proxy values during selected periods and climatic modes for the three studied Iberian Margin sediment cores. Table S4 also shows averaged differences between OH-GDGT-based SSTs and other biomarker-based SSTs. Table S5 shows biomarker-based SST latitudinal gradients along the Iberian Margin.

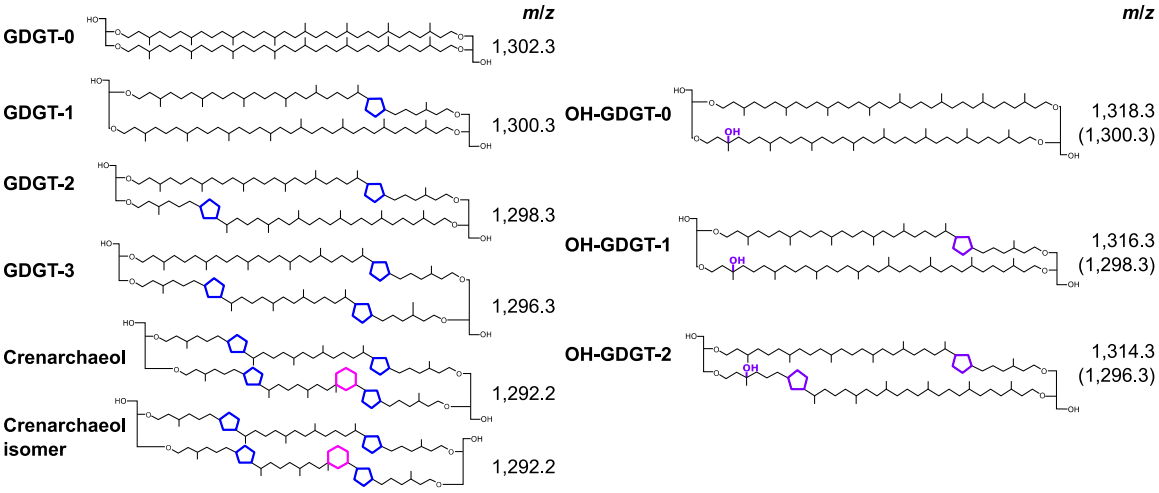

Figure S1. Structures of the archaeal glycerol dialkyl glycerol tetraethers (GDGTs) quantified in this study. Nonhydroxylated isoprenoid GDGTs are in the left column whereas hydroxylated isoprenoid GDGTs are in the right column. The written mass/charge (*m/z*) values of $[M+H]^+$ ions (protonated molecular ions) are the exact *m/z* values rounded to the first digit.

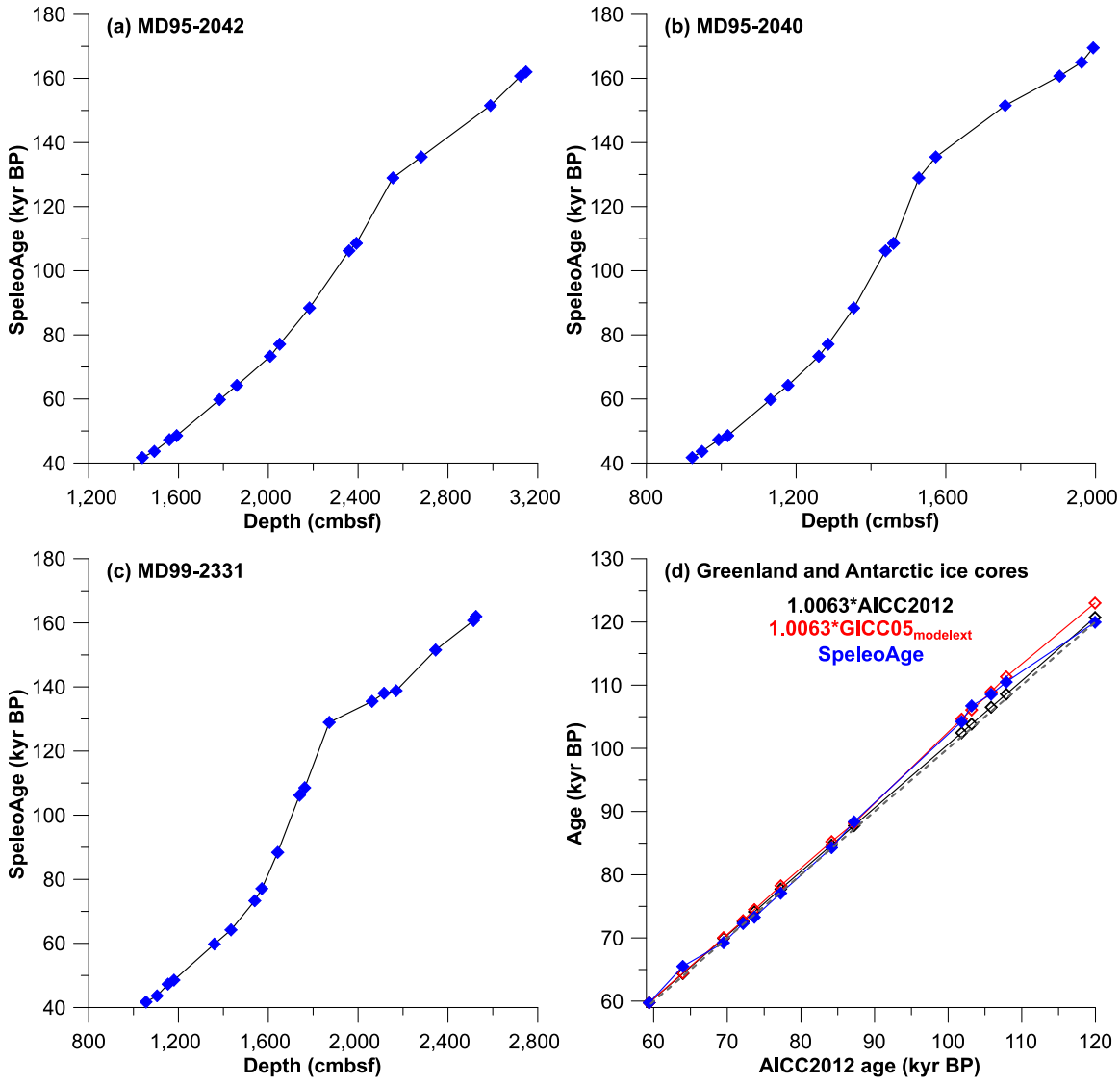

Figure S2. Tie points for synchronization to Chinese speleothems (SpeleoAge timescale). (a) Core MD95-2042. (b) Core MD95-2040. (c) Core MD99-2331. (d) Greenland and Antarctic ice cores. The linear scalings of Antarctic Ice Core Chronology 2012 (AICC2012; Bazin et al., 2013; Veres et al., 2013) and Greenland Ice Core Chronology 05$_{modelext}$ (GICC05$_{modelext}$; Wolff et al., 2010) timescales proposed by Buizert et al. (2015) are shown for comparison. Cmbsf = centimeters below sea floor.

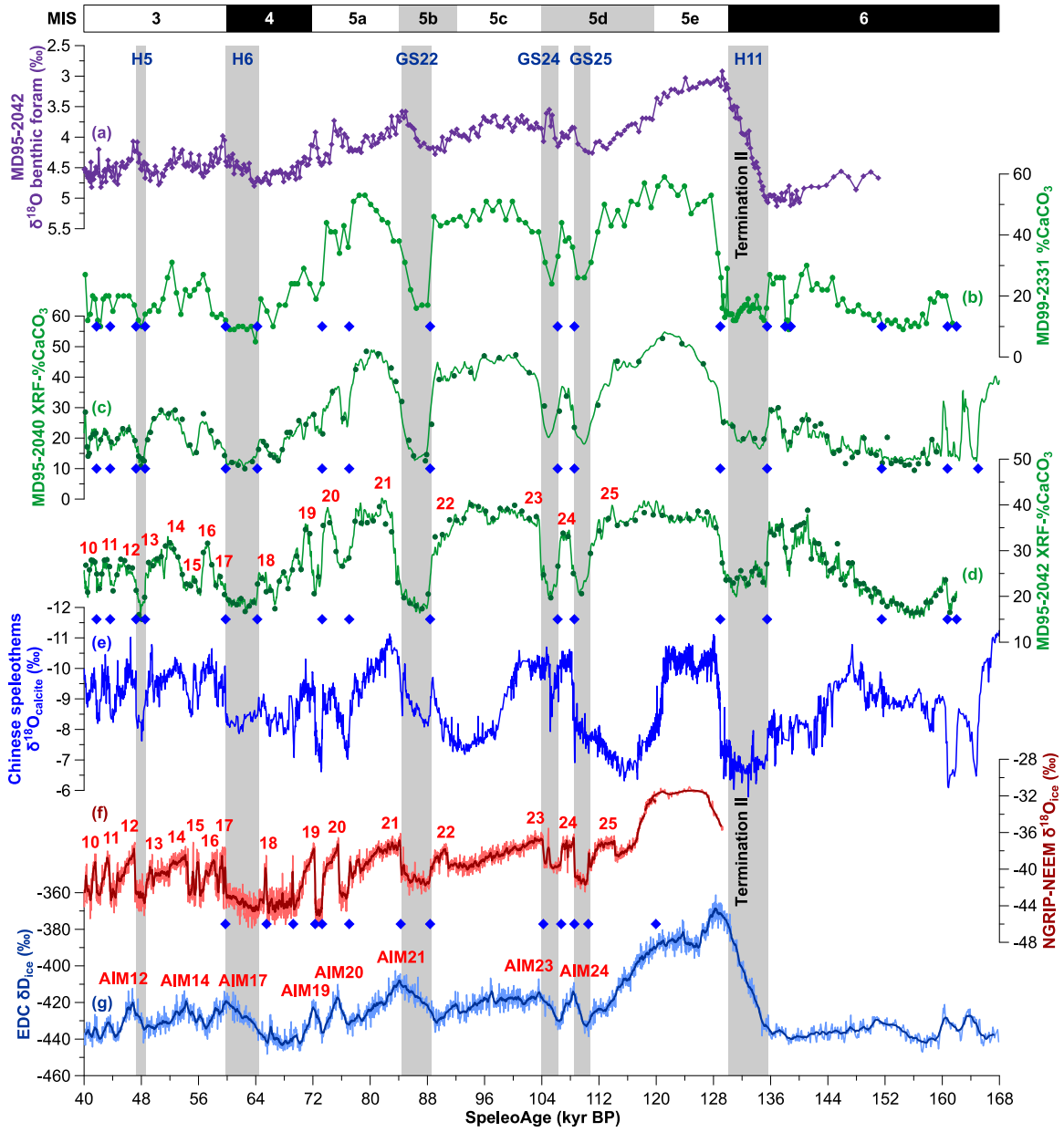

Figure S3. Synchronization to Chinese speleothems (SpeleoAge timescale). (a) Isotopic composition of oxygen ($\delta^{18}O$) of benthic foraminifers from core MD95-2042 (Shackleton et al., 2000): note the reversed axis. (b) Calcium carbonate content (%$CaCO_3$) from core MD99-2331 (Gouzy et al., 2004). (c) %$CaCO_3$ derived from X-ray fluorescence (XRF-%$CaCO_3$) from core MD95-2040 (this study) calibrated with measured %$CaCO_3$ (dark green circles; Thomson et al., 1999). (d) XRF-%$CaCO_3$ from core MD95-2042 (Darfeuil et al., 2016) calibrated with measured %$CaCO_3$ (dark green circles; Pailler & Bard, 2002). (e) $\delta^{18}O$ of calcite from Chinese speleothems (Cheng et al., 2016): note the reversed axis. (f) $\delta^{18}O$ of ice from the North Greenland Ice Core Project (NGRIP; NGRIP members, 2004) and North Greenland Eemian Ice Drilling (NEEM; NEEM community members, 2013) ice cores with 11-point moving averages (thick curves). (g) Isotopic composition of

hydrogen (δD) of ice from the European Project for Ice Coring in Antarctica Dome C (EDC; Jouzel et al., 2007) ice core with a 11-point moving average (thick curve). Only the 120–60 ka BP period of records in (f) and (g) is on the SpeleoAge timescale: their portion after 60 ka BP is on the Antarctic Ice Core Chronology 2012 (AICC2012) × 1.0063 timescale (Buizert et al., 2015; WAIS Divide Project Members, 2015) whereas their portion before 120 ka BP is on the AICC2012 timescale (Bazin et al., 2013; Veres et al., 2013). Blue diamonds in (b–d) and (f) are the tie points selected for synchronization to Chinese speleothems. Red numbers in (d) and (f) correspond to Dansgaard–Oeschger events. Red labels in (g) correspond to the most prominent Antarctic Isotopic Maxima (AIM). Grey bars with dark blue labels correspond to the most prominent Greenland stadials (GS22, GS24, and GS25) and Heinrich events (H5, H6, and H11). Marine isotope stages (MIS) are named according to Railsback et al. (2015) and defined based on the benthic foraminifer $\delta^{18}O$ record in (a).

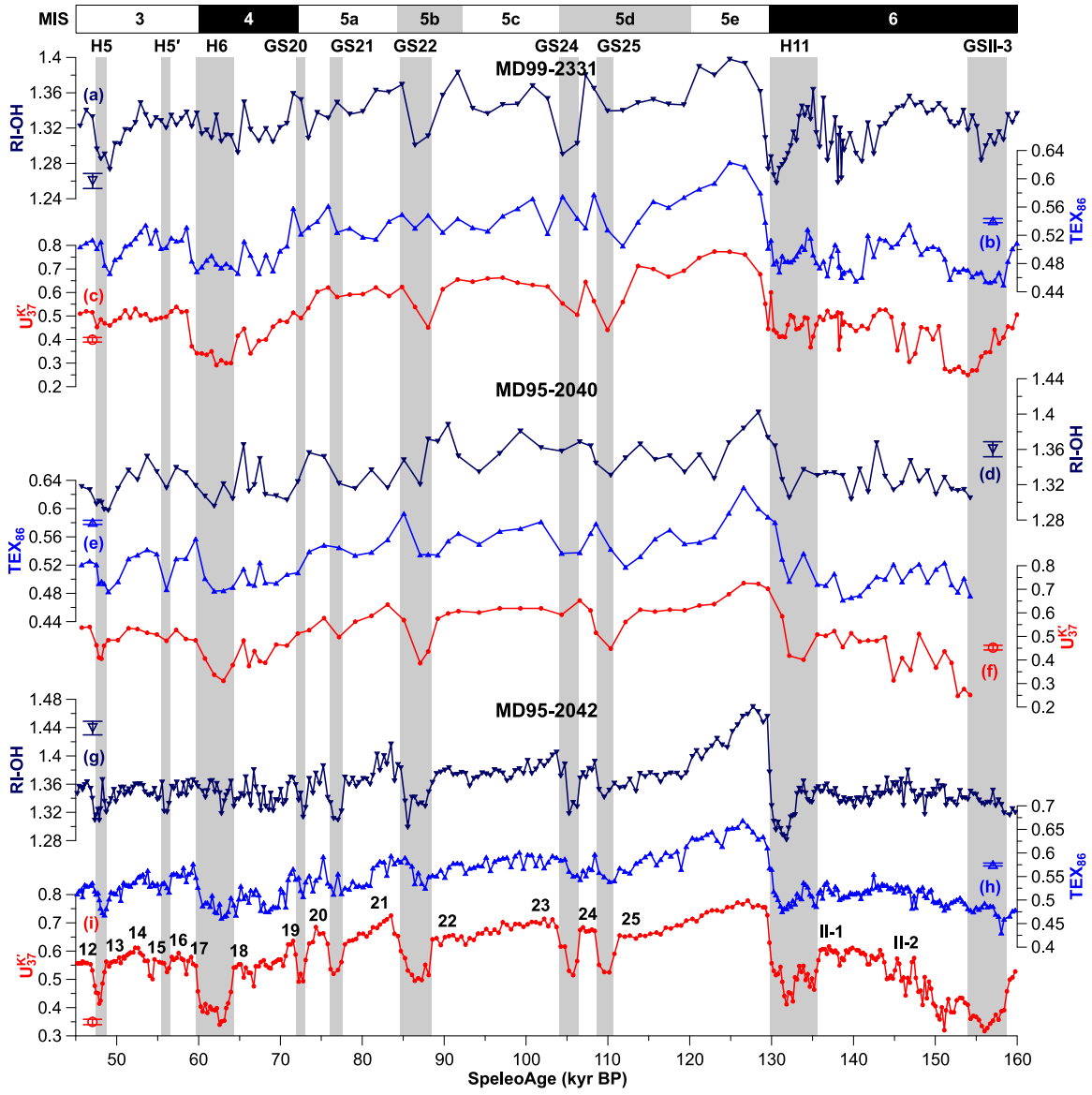

Figure S4. Same as Figure 2, but with RI-OH (ring index of hydroxylated tetraethers without OH-GDGT-0; Lü et al., 2015) records in dark blue instead of RI-OH' (ring index of hydroxylated tetraethers with OH-GDGT-0; Lü et al., 2015) records.

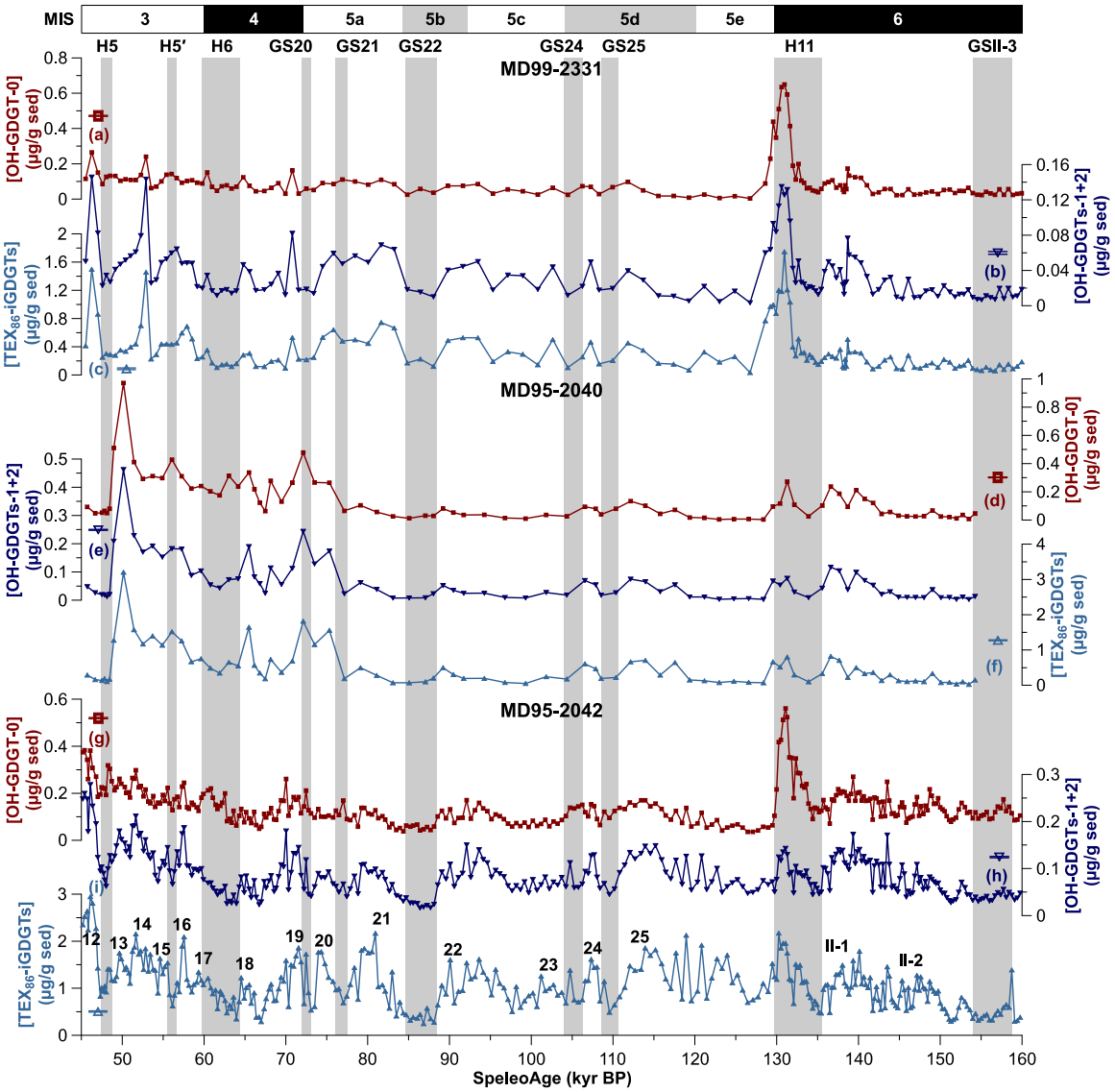

Figure S5. Same as Figure 3, but with biomarker concentration results for other lipid classes. Summed GDGT-1, GDGT-2, GDGT-3 and crenarchaeol isomer concentration records are in turquoise blue, summed OH-GDGT-1 and OH-GDGT-2 concentration records are in dark blue and OH-GDGT-0 concentration records are in dark red.

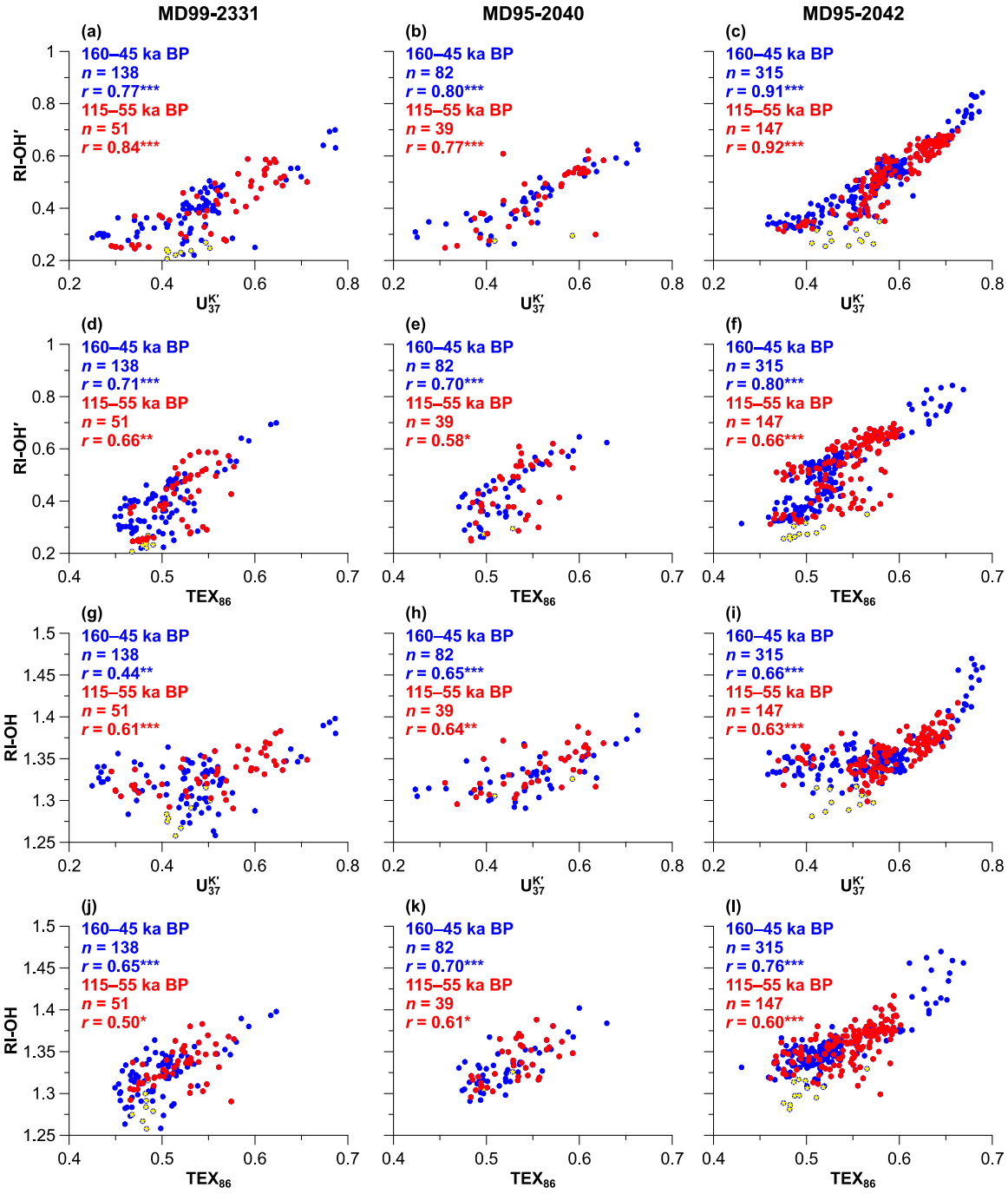

Figure S6. Correlations between organic paleothermometers for Iberian Margin cores MD99-2331, MD95-2040, and MD95-2042. (a–c) RI-OH′ versus $U^{K'}_{37}$. (d–f) RI-OH′ versus TEX_{86}. (g–i) RI-OH versus $U^{K'}_{37}$. (j–l) RI-OH versus TEX_{86}. Blue and red symbols refer to the 160–45 and 115–55 ka BP periods, respectively. Blue symbols with a yellow star refer to the 133–130 ka BP period, which corresponds to the primary productivity peak during the end of Heinrich event H11. Samples with only alkenone-based or tetraether-based data are omitted. Statistical significance levels (from a nonparametric method that accounts for serial correlation; Ebisuzaki, 1997) are coded as follows: * for $p < 0.05$, ** for

$p < 0.01$, and *** for $p < 0.001$. TEX_{86} = TetraEther indeX of tetraethers consisting of 86 carbon atoms (Schouten et al., 2002), $U^{K'}_{37}$ = C_{37} ketone unsaturation ratio (Prahl & Wakeham, 1987), and RI-OH and RI-OH′ = ring index of hydroxylated tetraethers (Lü et al., 2015).

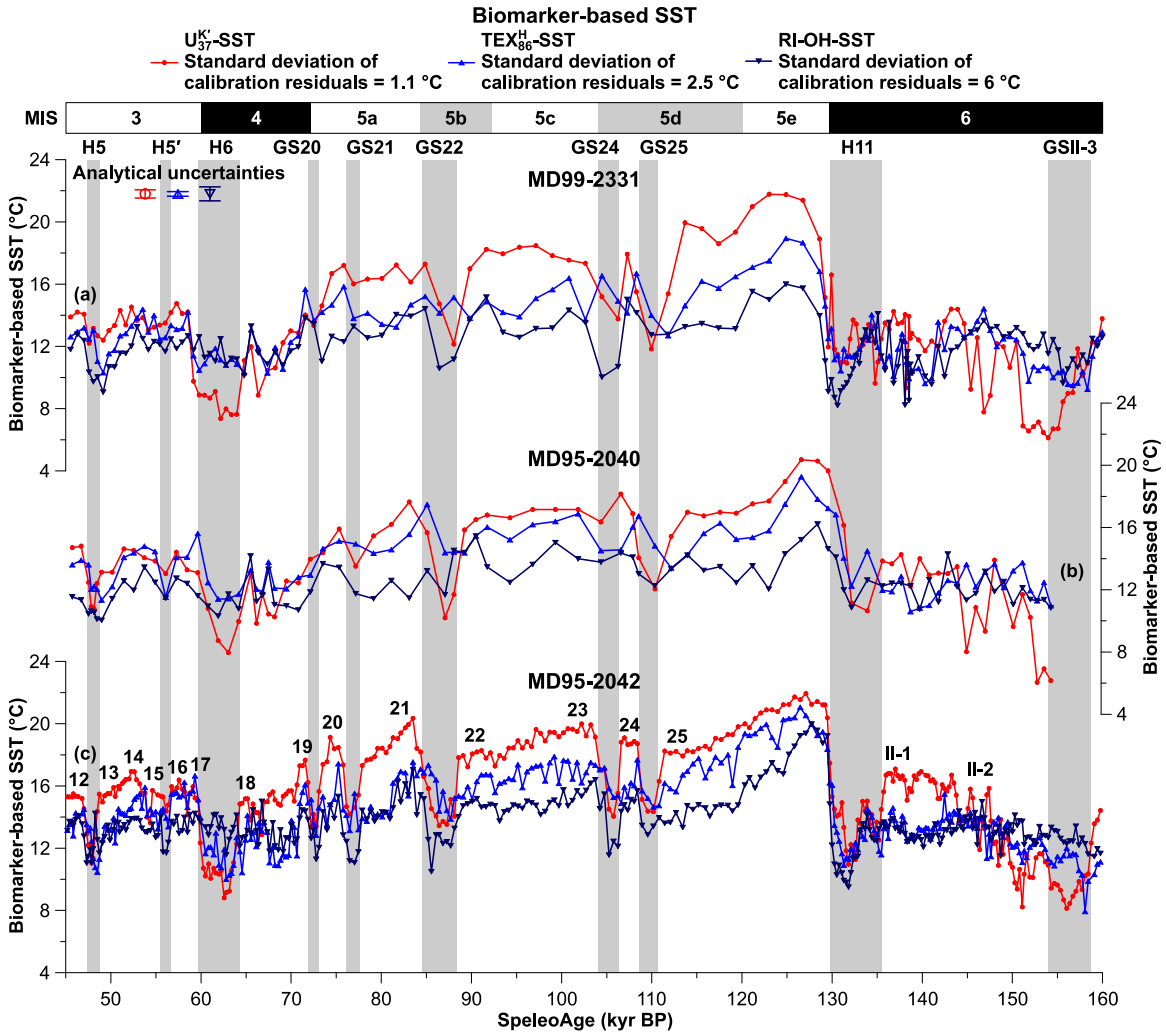

Figure S7. Same as Figure 5, but with RI-OH-SST estimates (ring index of hydroxylated tetraethers without OH-GDGT-0; Lü et al., 2015) instead of RI-OH'-SST estimates (ring index of hydroxylated tetraethers with OH-GDGT-0; Lü et al., 2015). RI-OH-SST estimates are based on the following global calibration: SST = (RI-OH − 1.11)/0.018 (Lü et al., 2015).

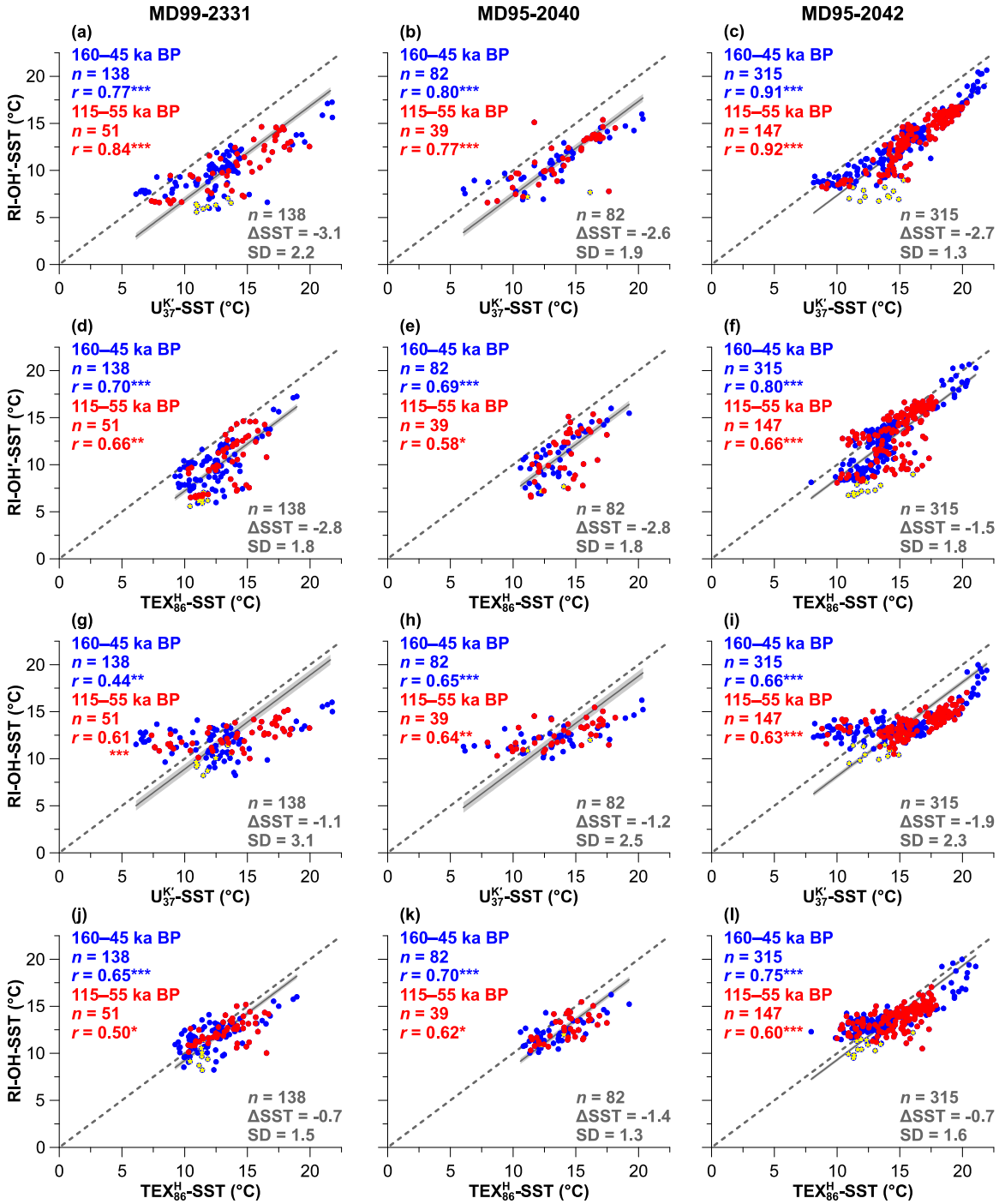

Figure S8. Same as Figure S6, but with comparisons of biomarker-based sea surface temperature (SST) estimates from Iberian Margin cores MD99-2331, MD95-2040, and MD95-2042. (a–c) RI-OH'-SSTs versus $U^{K'}_{37}$-SSTs. (d–f) RI-OH'-SSTs versus TEX_{86}^{H}-SSTs. (g–i) RI-OH-SSTs versus $U^{K'}_{37}$-SSTs. (j–l) RI-OH-SSTs versus TEX_{86}^{H}-SSTs. RI-OH'-SST estimates are based on the following global calibration: SST = (RI-OH' + 0.029)/0.0422 (Fietz et al., 2020). RI-OH-SST estimates are based on the following global calibration: SST = (RI-OH − 1.11)/0.018 (Lü et al., 2015). $U^{K'}_{37}$-SST estimates are based on the

following global calibration: SST = 29.876 × $U^{K'}_{37}$ − 1.334 (Conte et al., 2006). TEX_{86}^{H}-SST estimates are based on the following regional paleocalibration: SST = 68.4 × TEX_{86}^{H} + 33.0 (Darfeuil et al., 2016). Dashed lines indicate 1:1 relationships. Dark grey solid lines with grey shadings represent mean SST differences (ΔSST) with their 2σ standard errors for the 160–45 ka BP period, with accompanying ΔSST and 1σ standard deviation values. TEX_{86}^{H} = log(TEX_{86}) with TEX_{86} = TetraEther indeX of tetraethers consisting of 86 carbon atoms (Kim et al., 2010; Schouten et al., 2002).

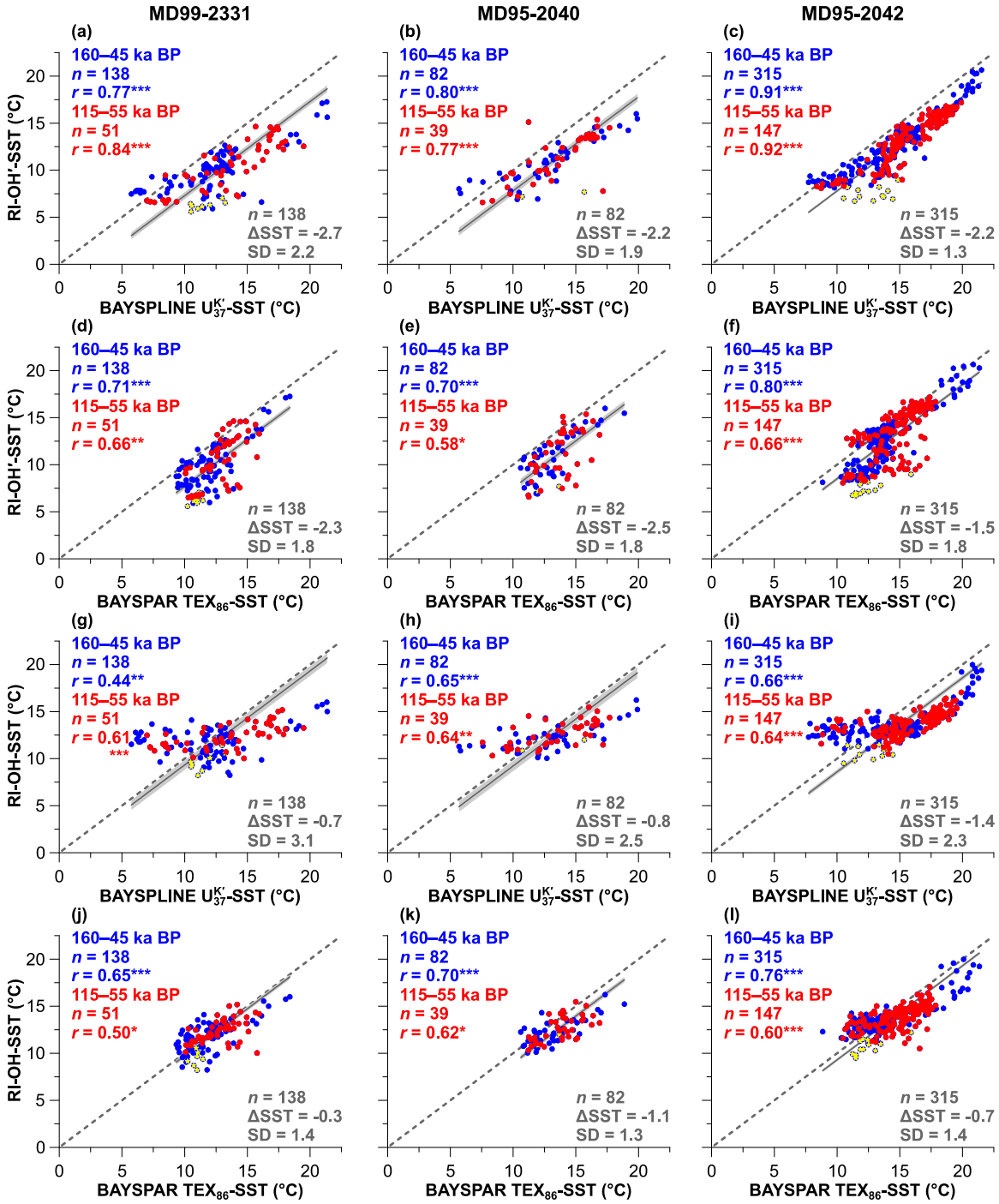

Figure S9. Same as Figure S8, but using Bayesian calibrations for $U^{K'}_{37}$-SST (Tierney & Tingley, 2018) and TEX_{86}-SST estimates (Tierney & Tingley, 2014, 2015). (a–c) RI-OH′-SSTs versus BAYSPLINE $U^{K'}_{37}$-SSTs. (d–f) RI-OH′-SSTs versus BAYSPAR TEX_{86}-SSTs. (g–i) RI-OH-SSTs versus BAYSPLINE $U^{K'}_{37}$-SSTs. (j–l) RI-OH-SSTs versus BAYSPAR TEX_{86}-SSTs. TEX_{86} = TetraEther indeX of tetraethers consisting of 86 carbon atoms (Schouten et al., 2002).

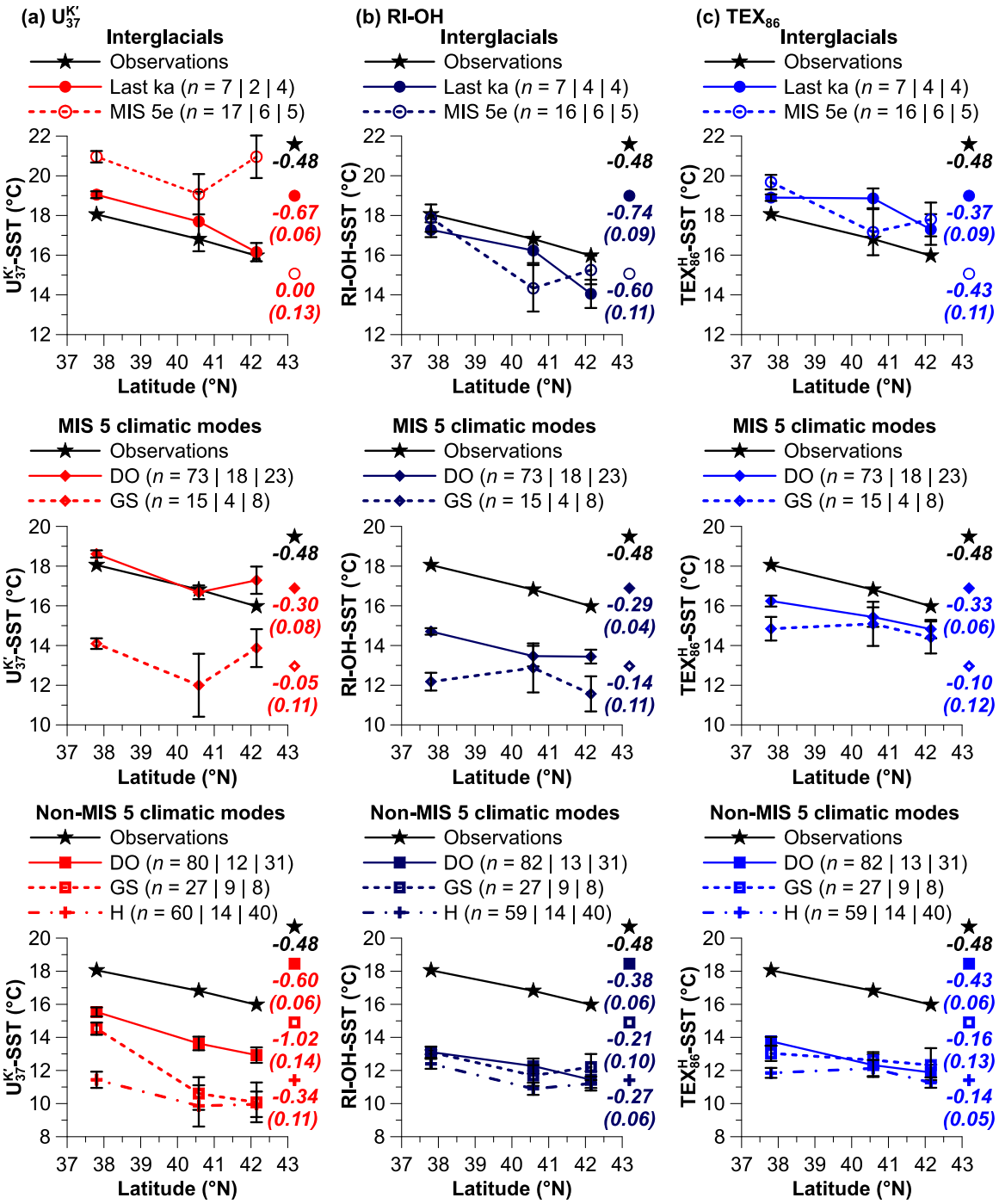

Figure S10. Same as Figure 6, but with RI-OH-SST estimates (ring index of hydroxylated tetraethers without OH-GDGT-0; Lü et al., 2015) in (b) instead of RI-OH'-SST estimates (ring index of hydroxylated tetraethers with OH-GDGT-0; Lü et al., 2015). RI-OH-SST estimates are based on the following global calibration: SST = (RI-OH − 1.11)/0.018 (Lü et al., 2015).

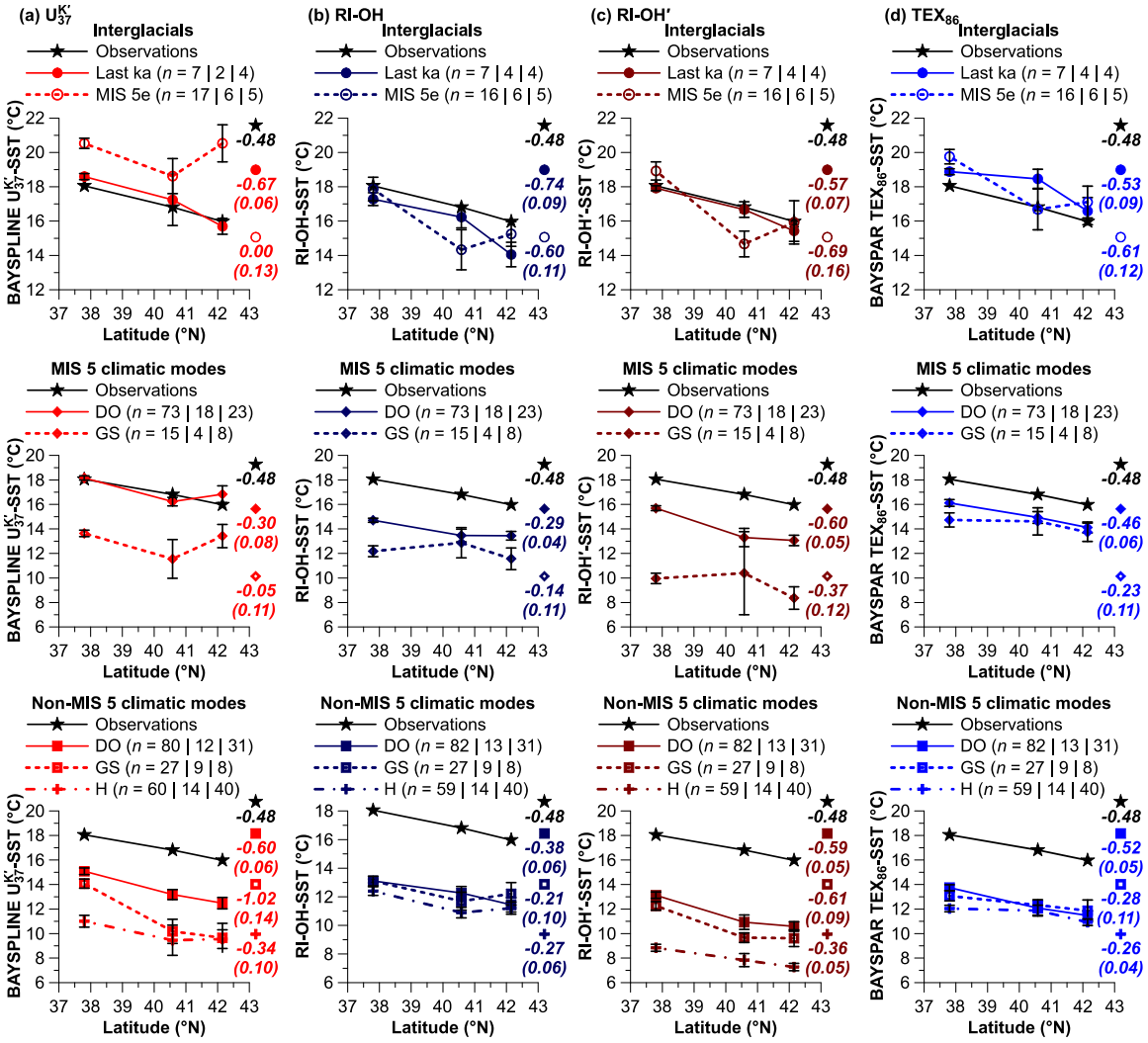

Figure S11. Same as Figures 6 and S10, but using Bayesian calibrations for $U^{K'}_{37}$-SST and TEX_{86}-SST estimates. (a) $U^{K'}_{37}$-SST estimates from the BAYSPLINE calibration (Tierney & Tingley, 2018). (b) RI-OH-SST estimates from the following global calibration: SST = (RI-OH − 1.11)/0.018 (Lü et al., 2015). (c) RI-OH'-SST estimates from the following global calibration: SST = (RI-OH' + 0.029)/0.0422 (Fietz et al., 2020). (d) TEX_{86}-SST estimates from spatially varying BAYSPAR calibration (Tierney & Tingley, 2014, 2015). TEX_{86} = TetraEther indeX of tetraethers consisting of 86 carbon atoms (Schouten et al., 2002).

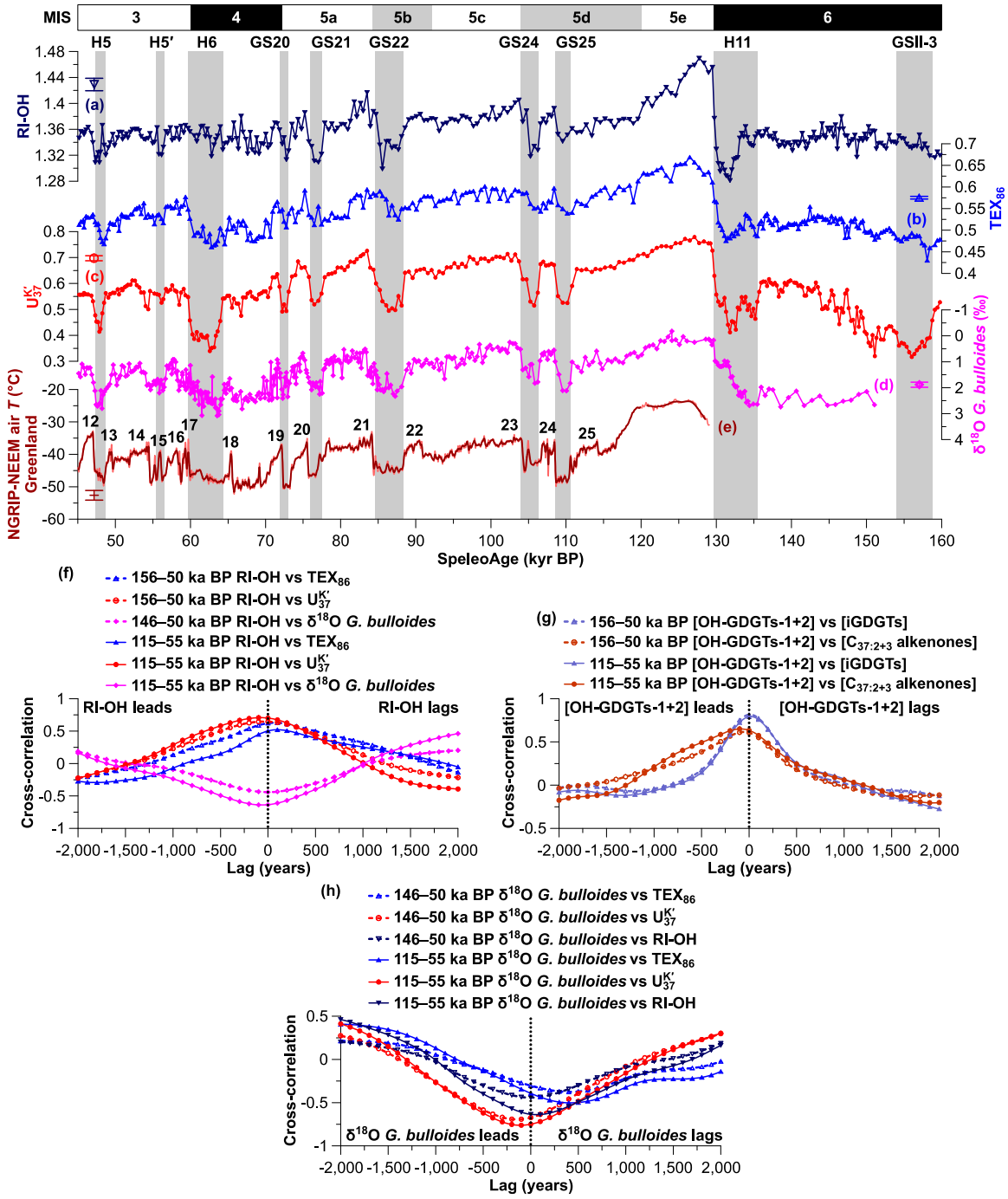

Figure S12. Same as Figure 7, but with RI-OH (ring index of hydroxylated tetraethers without OH-GDGT-0; Lü et al., 2015) in (a) instead of RI-OH′ (ring index of hydroxylated tetraethers with OH-GDGT-0; Lü et al., 2015) and with the considerations of RI-OH instead of RI-OH′ in (f) and (h) and of summed OH-GDGT-1 and OH-GDGT-2 concentrations instead of total OH-GDGT concentrations in (g).

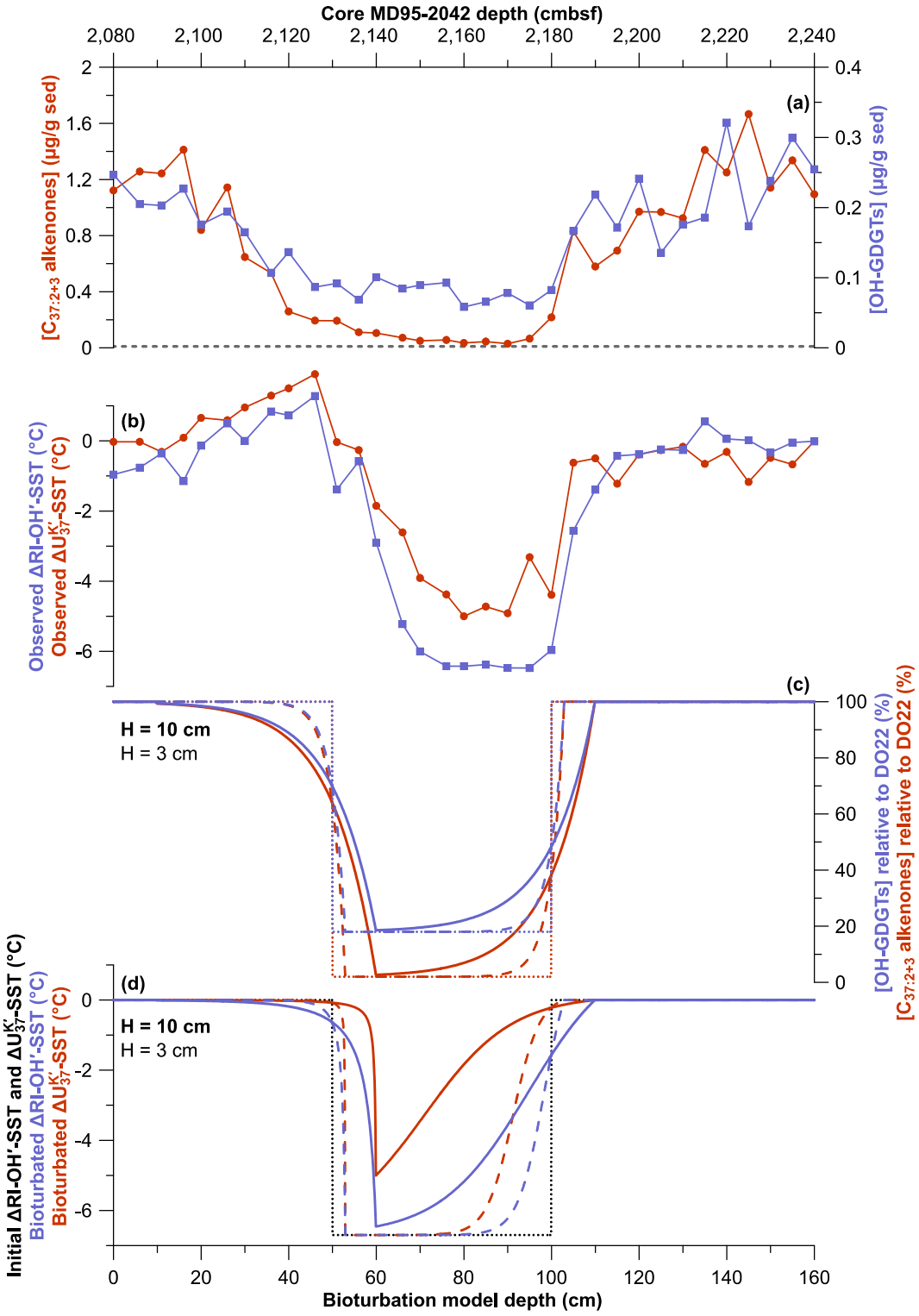

Figure S13. Observed and theoretical bioturbation effect on SST changes derived from RI-OH′ (ring index of hydroxylated tetraethers; Lü et al., 2015) and $U^{K'}_{37}$ (C_{37} ketone unsaturation index; Prahl & Wakeham, 1987) during the 94–80 ka BP period, which comprises the cold event GS22. (a) Total OH-GDGT (blue curve with squares) and

summed di-unsaturated and tri-unsaturated C_{37} alkenone (red curve with circles) concentrations from core MD95-2042. The grey dashed line indicates the zero-concentration value. (b) Observed RI-OH′-SST (blue curve with squares) and $U^{K'}_{37}$-SST (red curve with circles) anomalies relative to the warm event DO22 from core MD95-2042. (c) Initial (dotted curves) and bioturbated (solid and dashed curves) OH-GDGT (blue) and di-unsaturated and tri-unsaturated C_{37} alkenone (red) concentrations relative to the warm event DO22, with assumed initial concentration drops by 98% for di-unsaturated and tri-unsaturated C_{37} alkenones and by 82% for OH-GDGTs. (d) Initial biomarker-based SST anomalies (dashed black curve) and bioturbated RI-OH′-SST (blue curves) and $U^{K'}_{37}$-SST (red curves) anomalies, all relative to the warm event DO22 and with an assumed initial SST drop by 6.7 °C. The bioturbated signals were generated using the model by Bard, Arnold, Duprat, et al. (1987), with *H* (bioturbation depth) = 10 and 3 cm (solid and dashed curves, respectively) and *T* (sampling step) = 0.1 cm. Cmbsf = centimeters below sea floor, GDGT = glycerol dialkyl glycerol tetraether, DO = Dansgaard–Oeschger event, and GS = Greenland stadial.

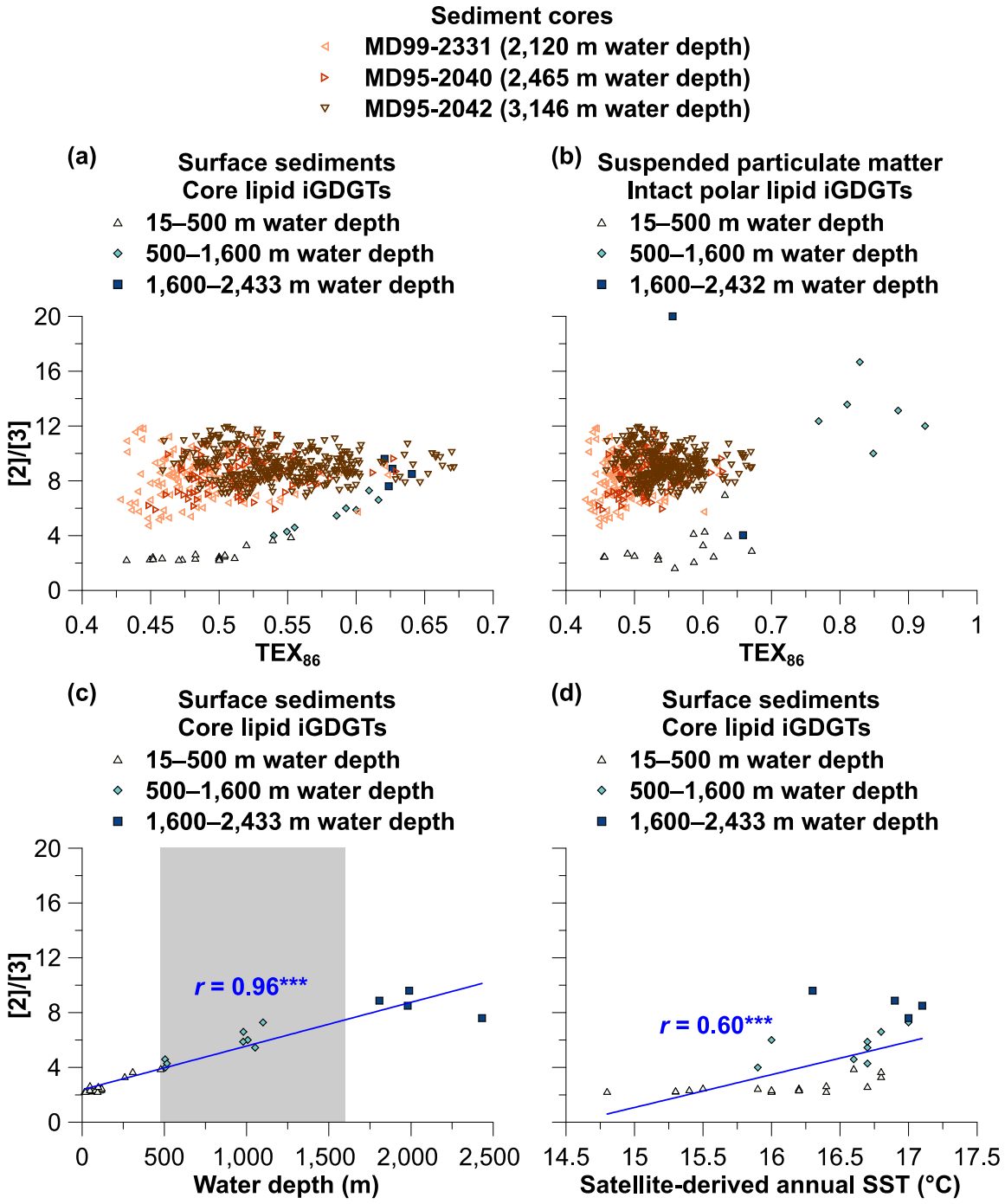

Figure S14. Correlations between GDGT-2/GDGT-3 ([2]/[3]) ratios and TEX_{86} and between [2]/[3] ratios and relevant environmental parameters for Iberian Margin cores MD99-2331, MD95-2040, and MD95-2042, as well as Iberian Margin surface sediments and suspended particulate matter. Modern samples taken above, within, and below the Mediterranean Outflow Waters (presently at 500–1,600 m water depth; Kim et al., 2016) are distinguished. (a) [2]/[3] ratio versus TEX_{86}, with a comparison of the studied Iberian Margin sediment cores with Iberian Margin surface sediments examined for core lipid iGDGTs by Kim et al. (2016). (b) Same as (a), but with a comparison of the studied Iberian

Margin sediment cores with Iberian Margin suspended particulate matter examined for intact polar lipid iGDGTs by Kim et al. (2016). (c) [2]/[3] ratio versus water depth for Iberian Margin surface sediments examined for core lipid iGDGTs by Kim et al. (2016). (d) Same as (c), but for [2]/[3] ratio versus satellite-derived annual sea surface temperature (SST). The statistical significance level of $p < 0.001$ in (c) and (d) is coded as ***.

Climatic event (names after Martrat et al., 2007)	MD95-2042 depth (cmbsf)	MD95-2040 depth (cmbsf)	MD99-2331 depth (cmbsf)	SpeleoAge Cheng et al. (2016) (kyr BP)
Start DO10	1,438.92	922.19	1,055.55	41.732
Start DO11	1,492.51	948.51	1,105.00	43.650
End H5 (Start DO12)	1,559.71	993.03	1,153.27	47.274
Start H5	1,591.83	1,017.51	1,180.00	48.532
End H6 (Start DO17)	1,782.85	1,131.57	1,360.00	59.796
Start H6 (End DO18)	1,859.44	1,178.36	1,434.17	64.213
End DO20	2,008.38	1,260.51	1,540.00	73.288
End DO21	2,050.51	1,285.51	1,571.25	77.078
End DO22	2,183.13	1,354.00	1,642.14	88.385
End DO24	2,359.51	1,438.85	1,739.53	106.215
Start DO24	2,392.01	1,460.01	1,762.50	108.552
Termination II	2,554.83	1,527.88	1,871.82	128.957
End DO1	2,680.83	1,573.00	2,062.24	135.501
Start DO1	N/A	N/A	2,115.42	138.031
End DO2	N/A	N/A	2,169.27	138.811
Start DO2 (after H event)	2,989.12	1,758.70	2,345.00	151.528
Start DO3	3,123.95	1,904.24	2,513.98	160.724
End DO4	3,147.43	N/A	2,524.71	162.001

Table S1. SpeleoAge tie points based on Cheng et al. (2016) and corresponding climatic events for the cores MD95-2042, MD95-2040, and MD99-2331. Cmbsf = centimeters below sea floor, DO = Dansgaard–Oeschger event, and H = Heinrich event. N/A = not available.

Climatic event	NGRIP depth (m)	GICC05$_{modelext}$ Wolff et al. (2010) (kyr BP)	AICC2012 Veres et al. (2013) (kyr BP)	SpeleoAge Cheng et al. (2016) (kyr BP)
Start DO17	2,420.35	59.385	59.388	59.760
Start DO18	2,465.84	64.049	63.958	65.505
End DO19	2,508.00	69.610	69.490	69.251
Start DO19	2,535.96	72.290	72.142	72.299
End DO20	2,547.38	74.030	73.679	73.288
End DO21	2,591.13	77.790	77.257	77.078
Start DO21	2,687.58	84.730	84.172	84.278
End DO22	2,717.75	87.610	87.220	88.385
Start DO23	2,891.53	103.990	101.819	104.215
End DO24	2,905.26	105.410	103.181	106.715
Start DO24	2,938.38	108.250	105.836	108.552
End DO25	2,954.42	110.630	107.892	110.500
Bottom of the ice core	3,084.73	122.230	119.952	119.952

Table S2. SpeleoAge (Cheng et al., 2016), Antarctic Ice Core Chronology 2012 (AICC2012; Bazin et al., 2013; Veres et al., 2013), and Greenland Ice Core Chronology 05$_{modelext}$ (GICC05$_{modelext}$; Wolff et al., 2010) tie points and corresponding climatic events for the North Greenland Ice Core Project (NGRIP; NGRIP members, 2004) ice core. DO = Dansgaard–Oeschger event.

Core	Period	*n* Alk/GDGT	RI-OH'		RI-OH		TEX_{86}		$U^{K'}_{37}$	
			Mean	SD	Mean	SD	Mean	SD	Mean	SD
MD31	1–0 ka BP	4/4	0.62	0.03	1.36	0.01	0.59	0.02	0.59	0.02
	MIS 5e	5/5	0.64	0.06	1.38	0.01	0.60	0.02	0.75	0.04
	MIS 5 DO	23/23	0.52	0.04	1.35	0.02	0.54	0.02	0.62	0.06
	MIS 5 GS	9/9	0.33	0.06	1.32	0.02	0.53	0.02	0.52	0.05
	Glacial MIS	58/58	0.41	0.05	1.32	0.02	0.50	0.02	0.47	0.05
	H	40/40	0.28	0.04	1.31	0.02	0.48	0.02	0.38	0.08
MD40	1–0 ka BP	2/4	0.67	0.02	1.40	0.01	0.62	0.01	0.64	0.04
	MIS 5e	6/6	0.59	0.04	1.37	0.03	0.59	0.03	0.68	0.04
	MIS 5 DO	20/20	0.53	0.07	1.35	0.02	0.55	0.02	0.60	0.03
	MIS 5 GS	7/7	0.43	0.12	1.34	0.02	0.54	0.02	0.49	0.07
	Glacial MIS	34/35	0.42	0.05	1.33	0.02	0.51	0.02	0.47	0.06
	H	14/14	0.30	0.04	1.31	0.01	0.50	0.02	0.37	0.08
MD42	1–0 ka BP	7/7	0.73	0.01	1.42	0.01	0.62	<0.01	0.68	0.01
	MIS 5e	17/16	0.77	0.04	1.43	0.02	0.64	0.02	0.75	0.02
	MIS 5 DO	73/73	0.63	0.04	1.37	0.01	0.57	0.02	0.67	0.03
	MIS 5 GS	15/15	0.39	0.03	1.33	0.02	0.54	0.02	0.52	0.02
	Glacial MIS	136/137	0.50	0.06	1.35	0.01	0.52	0.02	0.54	0.06
	H	60/59	0.34	0.05	1.33	0.02	0.49	0.02	0.43	0.06

Table S3. RI-OH' (ring index of hydroxylated tetraethers with OH-GDGT-0; Lü et al., 2015), RI-OH (ring index of hydroxylated tetraethers without OH-GDGT-0; Lü et al., 2015), TEX_{86} (TetraEther indeX of tetraethers consisting of 86 carbon atoms; Schouten et al., 2002), and $U^{K'}_{37}$ (C_{37} ketone unsaturation ratio; Prahl & Wakeham, 1987) averaged values during selected periods and climatic modes from Iberian Margin cores MD99-2331 (MD31), MD95-2040 (MD40), and MD95-2042 (MD42). MIS 5e corresponds to the thermal optimum during the 129–121, 130–121, and 129.5–120.3 ka BP periods for cores MD99-2331, MD95-2040, and MD95-2042, respectively. MIS 5e is excluded from MIS 5 DO. Glacial MIS correspond to MIS 6, 4, and 3. Heinrich events (GSII-3, H11, H6, and H5) are excluded from glacial MIS and are thus considered separately. Further details concerning the data points selected for each period and climatic mode are provided in Data Sets S1–S3 (column "Data points for averaged values"). Alk = alkenone, GDGT = glycerol dialkyl glycerol tetraether, MIS = marine isotope stage, DO = Dansgaard–Oeschger events, GS = Greenland stadials, H = Heinrich events, and SD = standard deviation.

		160–45 ka BP					115–55 ka BP	
Relationship	Core	*n*	*r*	ΔSST	BAY-ΔSST	ΔsubT	*n*	*r*
RI-OH′	MD99-2331	138	0.77***	–3.1 (2.2)	–2.7 (2.2)	N/A	51	0.84***
versus $U^{K'}_{37}$	MD95-2040	82	0.80***	–2.6 (1.9)	–2.2 (1.9)	N/A	39	0.77***
	MD95-2042	315	0.91***	–2.7 (1.3)	–2.2 (1.3)	N/A	147	0.92***
RI-OH′	MD99-2331	138	0.71***	–2.8 (1.8)	–2.3 (1.8)	–0.7 (1.8)	51	0.66**
versus TEX_{86}	MD95-2040	82	0.70***	–2.8 (1.8)	–2.5 (1.8)	–0.8 (1.8)	39	0.58*
	MD95-2042	315	0.80***	–1.5 (1.8)	–1.5 (1.8)	–0.2 (1.8)	147	0.66***
RI-OH	MD99-2331	138	0.44**	–1.1 (3.1)	–0.7 (3.1)	N/A	51	0.61***
versus $U^{K'}_{37}$	MD95-2040	82	0.65***	–1.2 (2.5)	–0.8 (2.5)	N/A	39	0.64**
	MD95-2042	315	0.66***	–1.9 (2.3)	–1.4 (2.3)	N/A	147	0.63***
RI-OH	MD99-2331	138	0.65***	–0.7 (1.5)	–0.3 (1.4)	1.3 (1.4)	51	0.50*
versus TEX_{86}	MD95-2040	82	0.70***	–1.4 (1.3)	–1.1 (1.3)	0.6 (1.2)	39	0.61*
	MD95-2042	315	0.76***	–0.7 (1.6)	–0.7 (1.4)	1.0 (1.4)	147	0.60***

Table S4. RI-OH′ and RI-OH versus $U^{K'}_{37}$ and TEX_{86} relationships for Iberian Margin cores MD99-2331, MD95-2040, and MD95-2042. Mean SST differences (ΔSST and BAY-ΔSST) with their 1σ standard deviations in brackets are also shown for the 160–45 ka BP period. Both non-Bayesian (ΔSST; after Conte et al., 2006; Darfeuil et al., 2016; Fietz et al., 2020; Lü et al., 2015) and Bayesian (BAY-ΔSST; after Fietz et al., 2020; Lü et al., 2015; Tierney & Tingley, 2014, 2015, 2018) SST estimates are considered for TEX_{86} and $U^{K'}_{37}$. RI-OH′-based and RI-OH-based SST estimates are also compared with Bayesian TEX_{86}-based 0- to 200-m sea temperature (gamma function probability distribution for target temperatures with a = 4.5 and b = 15) estimates (ΔsubT; after Fietz et al., 2020; Lü et al., 2015; Tierney & Tingley, 2014, 2015). Samples with only alkenone-based or tetraether-based data are omitted. Statistical significance levels (from a nonparametric method that accounts for serial correlation; Ebisuzaki, 1997) are coded as follows: * for $p < 0.05$, ** for $p < 0.01$, and *** for $p < 0.001$. TEX_{86} = TetraEther indeX of tetraethers consisting of 86 carbon atoms (Schouten et al., 2002), $U^{K'}_{37}$ = C_{37} ketone unsaturation ratio (Prahl & Wakeham, 1987), RI-OH and RI-OH′ = ring index of hydroxylated tetraethers (Lü et al., 2015), and N/A = not applicable.

	Biomarker-based SST latitudinal gradient (°C/°latitude)					
Period	RI-OH′	RI-OH	TEX_{86}^{H}	BAY-TEX_{86}	$U^{K'}_{37}$	BAY-$U^{K'}_{37}$
1–0 ka BP	–0.57	–0.74	–0.37	–0.53	–0.67	–0.67
	(0.07)	(0.09)	(0.09)	(0.09)	(0.06)	(0.06)
MIS 5e	–0.69	–0.60	–0.43	–0.61	0.00	0.00
	(0.16)	(0.11)	(0.11)	(0.12)	(0.13)	(0.13)
MIS 5 DO	–0.60	–0.29	–0.33	–0.46	–0.30	–0.30
	(0.05)	(0.04)	(0.06)	(0.06)	(0.08)	(0.08)
MIS 5 GS	–0.37	–0.14	–0.10	–0.23	–0.05	–0.05
	(0.12)	(0.11)	(0.12)	(0.11)	(0.11)	(0.11)
Non-MIS 5 DO	–0.59	–0.38	–0.43	–0.52	–0.60	–0.60
	(0.05)	(0.06)	(0.06)	(0.05)	(0.06)	(0.06)
Non-MIS 5 GS	–0.61	–0.21	–0.16	–0.28	–1.02	–1.02
	(0.09)	(0.10)	(0.13)	(0.11)	(0.14)	(0.14)
H	–0.36	–0.27	–0.14	–0.26	–0.34	–0.34
	(0.05)	(0.06)	(0.05)	(0.04)	(0.11)	(0.10)

Table S5. Comparison of biomarker-based sea surface temperature (SST) latitudinal gradients. Biomarker-based SST latitudinal gradients and propagated 1σ standard errors in brackets correspond to differences between cores MD99-2331 and MD95-2042. RI-OH′-SST estimates are from the following global calibration: SST = (RI-OH′ + 0.029)/0.0422 (Fietz et al., 2020). RI-OH-SST estimates are from the following global calibration: SST = (RI-OH − 1.11)/0.018 (Lü et al., 2015). TEX_{86}^{H}-SST estimates are from the following regional paleocalibration: SST = 68.4 × TEX_{86}^{H} + 33.0 (Darfeuil et al., 2016). BAY-TEX_{86}-SST estimates are from the BAYSPAR calibration (Tierney & Tingley, 2014, 2015). $U^{K'}_{37}$-SST estimates are from the following global calibration: SST = 29.876 × $U^{K'}_{37}$ − 1.334 (Conte et al., 2006). BAY-$U^{K'}_{37}$-SST estimates are from the BAYSPLINE calibration (Tierney & Tingley, 2018). MIS 5e corresponds to the thermal optimum during the 129–121, 130–121, and 129.5–120.3 ka BP periods for cores MD99-2331, MD95-2040, and MD95-2042, respectively. MIS 5e is excluded from MIS 5 DO. MIS = marine isotope stage, DO = Dansgaard–Oeschger events, GS = Greenland stadials, and H = Heinrich events. TEX_{86}^{H} = log(TEX_{86}) with TEX_{86} = TetraEther indeX of tetraethers consisting of 86 carbon atoms (Kim et al., 2010; Schouten et al., 2002), $U^{K'}_{37}$ = C_{37} ketone unsaturation ratio (Prahl & Wakeham, 1987), and RI-OH and RI-OH′ = ring index of hydroxylated tetraethers (Lü et al., 2015).

Data Set S1. Biomarker metadata and data for core MD99-2331: depth, age, summed OH-GDGT, iGDGT, and di-unsaturated and tri-unsaturated C_{37} alkenone concentrations, OH-GDGT-based, iGDGT-based, and alkenone-based paleothermometric indices, GDGT-2/GDGT-3 ratio, and biomarker-based sea surface temperature (SST) and 0- to 200-m sea temperature (subT; gamma function probability distribution for target temperatures with a = 4.5 and b = 15) estimates. The 1σ analytical uncertainties are 0.008 (0.5 °C) for RI-OH, 0.007 (0.2 °C) for RI-OH′, 0.003 (0.1 °C) for TEX_{86}, 0.263 for GDGT-2/GDGT-3, and 0.010 (0.26 °C) for $U^{K'}_{37}$. RI-OH′-SST estimates are from the following global calibration: SST = (RI-OH′ + 0.029)/0.0422 (Fietz et al., 2020). RI-OH-SST estimates are from the following global calibration: SST = (RI-OH − 1.11)/0.018 (Lü et al., 2015). TEX_{86}^{H}-SST estimates are from the following regional paleocalibration: SST = 68.4 × TEX_{86}^{H} + 33.0 (Darfeuil et al., 2016). $U^{K'}_{37}$-SST estimates are from the following global calibration: SST = 29.876 × $U^{K'}_{37}$ − 1.334 (Conte et al., 2006). Bayesian calibrations were also used for TEX_{86}-SST and TEX_{86}-subT estimates (BAYSPAR; Tierney & Tingley, 2014, 2015) and for $U^{K'}_{37}$-SST estimates (BAYSPLINE; Tierney & Tingley, 2018). Cmbsf = centimeters below sea floor, MIS = marine isotope stage, DO = Dansgaard–Oeschger event, GS = Greenland stadial, H = Heinrich event, GDGT = glycerol dialkyl glycerol tetraether, and N/A = not available.

Data Set S2. Same as Data Set S1, but for core MD95-2040. Core MD95-2040 $U^{K'}_{37}$ and summed di-unsaturated and tri-unsaturated C_{37} alkenone concentration data are from Pailler and Bard (2002).

Data Set S3. Same as Data Set S1, but for core MD95-2042. Core MD95-2042 $U^{K'}_{37}$ and summed di-unsaturated and tri-unsaturated C_{37} alkenone concentration data covering the 70–45 ka BP period are from Darfeuil et al. (2016).

Data Set S4. Cross-correlation results for core MD95-2042. A fourth-order Butterworth band-pass filter (500–10,000-year window) was applied to all evenly resampled (every 10 years) core MD95-2042 records before generating the cross-correlograms.